

Isochronous mass spectrometry at the RIKEN Rare-RI Ring facility

D. Nagae,^{1,2,3,*} S. Omika,^{4,1} Y. Abe,¹ Y. Yamaguchi,¹ F. Suzaki,^{1,5} K. Wakayama,⁴
 N. Tadano,⁴ R. Igosawa,⁴ K. Inomata,⁴ H. Arakawa,⁴ K. Nishimuro,⁴ T. Fujii,⁴
 T. Mitsui,⁴ T. Yamaguchi,^{4,6} T. Suzuki,⁴ S. Suzuki,⁷ T. Moriguchi,⁷ M. Amano,⁷
 D. Kamioka,⁷ A. Ozawa,⁷ S. Naimi,¹ Z. Ge,^{1,4} Y. Yanagisawa,¹ H. Baba,¹ S. Michimasa,⁸
 S. Ota,⁸ G. Lorusso,⁹ Yu.A. Litvinov,¹⁰ M. Wakasugi,¹ T. Uesaka,¹ and Y. Yano¹

¹*RIKEN Nishina Center, RIKEN, 2-1 Hirosawa,
 Wako-shi, Saitama 351-0198, Japan*

²*Research Center for SuperHeavy Elements,
 Kyushu University, 744 Motooka, Nishi-ku,
 Fukuoka-shi, Fukuoka 819-0395, Japan*

³*Laboratory for Zero-Carbon Energy,
 Tokyo Institute of Technology, 2-12-1 Ookayama,
 Meguro-ku, Tokyo 152-8550, Japan*

⁴*Department of Physics, Saitama University, Shimo-Okubo 255,
 Sakura-ku Saitama-shi, Saitama, 338-8570 Japan*

⁵*Advanced Science Research Center,
 Japan Atomic Energy Agency, 2-4 Shirakata,
 Tokai-mura, Naka-gun, Ibaraki 319-1195, Japan*

⁶*Tomonaga Center for the History of the Universe,
 University of Tsukuba, 1-1-1 Tennodai,
 Tsukuba-shi, Ibaraki, 305-8571, Japan*

⁷*Institute of Physics, University of Tsukuba,
 1-1-1 Tennodai, Tsukuba-shi, Ibaraki 305-8571, Japan*

⁸*Center for Nuclear Study, The University of Tokyo,
 2-1 Hirosawa, Wako, Saitama 351-0198, Japan*

⁹*Department of Physics, University of Surrey,
 Guildford, Surrey GU2 7XH, United Kingdom*

¹⁰*GSI Helmholtzzentrum für Schwerionenforschung GmbH,*

Planckstraße 1, 64291 Darmstadt, Germany

(Dated: July 9, 2024)

Abstract

A dedicated isochronous storage ring, named the Rare-RI Ring, was constructed at the RI Beam Factory of RIKEN, aiming at precision mass measurements of nuclei located in uncharted territories of the nuclear chart. The Rare-RI Ring employs the isochronous mass spectrometry technique with the goal to achieve a relative mass precision of 10^{-6} within a measurement time of less than 1 ms. The performance of the facility was demonstrated through mass measurements of neutron-rich nuclei with well-known masses. Velocity or magnetic rigidity is measured for every particle prior to its injection into the ring, wherein its revolution time is accurately determined. The latter quantity is used to determine the mass of the particle, while the former one is needed for non-isochronicity corrections. Mass precisions on the order of 10^{-5} were achieved in the first commissioning, which demonstrates that Rare-RI Ring is a powerful tool for mass spectrometry of short-lived nuclei.

I. INTRODUCTION

Mass is a fundamental quantity of an atomic nucleus which directly reflects its binding energy. Systematic studies of nuclear masses reveal information regarding the evolution of nuclear structure such as shell closures, changes of shapes, nucleon-nucleon correlations, weak and electromagnetic interactions, the equation of state for nuclear matter, and borders of nuclear existence [1]. Nuclear masses are particularly important for modeling the processes of synthesis of chemical elements in stellar environments [2]. Data on nuclear masses are nearly complete for most of the nucleosynthesis processes with the exception of the rapid neutron capture process (r process) [3]. The r process occurs in violent stellar events characterized by a high neutron density. Presently favored are binary neutron star mergers, which is supported by the identification of strontium in the lightcurve analysis [4] of so far the only observed kilonova AT2017gfo [5, 6], which is related to the gravitational wave detection GW170817 [7]. Numerous rapid captures of free neutrons drive matter towards the neutron drip line. Therefore, the nuclei involved in the r process are extremely neutron rich and as a rule short lived. The neutron capture and photodisintegration reaction rates critically depend on the neutron separation energy, which is the difference of masses of the corresponding parent and daughter nuclei and a free neutron. Sensitivity studies of

* nagae.d.aa@m.titech.ac.jp

r -process simulations for uncertainties of nuclear masses [8–10] indicate that masses need to be known with accuracy of better than $100 \text{ keV}/c^2$.

Various approaches developed for precision mass measurements of exotic nuclei [1] include Penning traps [11–15], multi-reflection time-of-flight mass spectrographs [16–19], and heavy-ion storage rings [20–23]. Altogether, a vast amount of mass data was provided for both neutron-rich and neutron-deficient nuclei [1]. In some cases uncertainties of the mass values can reach sub-keV level. However, precise mass measurements of exotic nuclei relevant for the r process remain challenging due to their short lifetimes and vanishingly small production rates. Only a few successful measurements have been reported so far; see, e.g., [24–29].

The RIKEN RI Beam Factory (RIBF) is an accelerator complex consisting of several linacs and cyclotrons [30]. The RIBF is currently the most powerful radioactive isotope (RI) beam production facility, giving access to many neutron-rich nuclei in the vicinity of the r process. To profit from this RIBF capability, a special cyclotron-like storage ring, named the Rare-RI Ring, was constructed at RIBF [31]. The Rare-RI Ring is designed to conduct mass measurements by utilizing isochronous mass spectrometry. The envisioned relative mass precision is $\delta m/m \approx 10^{-6}$. Since the measurement time is approximately 1 ms, the technique is quick enough to cover basically all relevant nuclear species.

Driving accelerators at other existing heavy-ion storage rings—ESR at GSI [32], and CSRe at IMP [33]—are heavy-ion synchrotrons. Synchrotrons and storage rings are synchronized and operate with bunched beams ejected and/or injected within one revolution in both machines [34]. Thus, the entire beam is ejected within several hundred nanoseconds. Neither particle identification nor velocity determination are feasible in the beam-line and have thus to be done inside the ring, which is often challenging [35–41].

In contrast, the Rare-RI Ring is coupled to a cyclotron. The quasicontinuous beam structure makes possible, by utilizing commonly used timing, tracking and ionization detectors, the particle identification as well as velocity measurement of every ion prior to its injection into the ring. However, the very short injection time effectively picks out only a single ion from the beam. Since various particles are produced in nuclear reactions at random times, the injection must be synchronized only with an ion of interest, which requires its prior identification. All of these were realized in a special individual-ion injection method, initially proposed in Ref. [42].

In the present study, we report the first commissioning mass measurements using nuclei

with well-known masses as well as the developed analysis methods. The first mass measurements at the storage ring in RIKEN were reported by us in Ref. [43]. That measurement became possible after a thorough characterization and development of the corresponding instrumentation. In the present work we report the details of the employed experimental technique and the initial commissioning results.

II. PRINCIPLE OF MASS MEASUREMENTS

In the isochronous mass spectrometry, an isochronous condition (isochronism) of the storage-ring optics is tuned using a reference nucleus whose rest mass m_0 is well known. As a result, the revolution times of the reference particles T_0 with the mass-to-charge ratio m_0/q_0 are constant, and are independent of their momenta. They are given by

$$T_0 = 2\pi \frac{m_0}{q_0} \frac{1}{B_0}, \quad (1)$$

where B_0 is the magnetic flux density. For a nucleus of interest with a mass-to-charge ratio $m_1/q_1 = m_0/q_0 \pm \Delta(m/q)$, the isochronism is not fulfilled [44]. The corresponding revolution times T_1 depend on particle momenta and the distribution of T_1 rapidly becomes wider with increasing $\Delta(m/q)$. It is assumed that ions with the same magnetic rigidities $B\rho$ have identical mean orbit lengths in the ring. If one of these ions is a reference, the following equations are satisfied:

$$B\rho = \frac{m_0}{q_0} \beta_0 \gamma_0 c = \frac{m_1}{q_1} \beta_1 \gamma_1 c, \quad (2)$$

$$\beta_0 T_0 = \beta_1 T_1, \quad (3)$$

where $\beta_{0,1}$ and $\gamma_{0,1}$ are the velocity in units of light speed c and the relativistic Lorentz factor, respectively. The subscripts 0 and 1 label the reference nucleus and the nucleus of interest, respectively. The mass-to-charge ratio m_1/q_1 can be derived from Eqs. (2) and (3) as follows:

$$\begin{aligned} \frac{m_1}{q_1} &= \frac{m_0}{q_0} \frac{T_1}{T_0} \frac{\gamma_0}{\gamma_1} \\ &= \frac{m_0}{q_0} \frac{T_1}{T_0} \sqrt{\frac{1 - \beta_1^2}{1 - \left\{ \left(\frac{T_1}{T_0} \right) \beta_1 \right\}^2}} \\ &= \frac{m_0}{q_0} \frac{T_1'}{T_0}, \end{aligned} \quad (4)$$

where T_1' denotes T_1 corrected by β_1 . This correction is indispensable and directly affects the attainable mass precision. The relative differential of m_1/q_1 is given as:

$$\begin{aligned}\frac{\delta(m_1/q_1)}{m_1/q_1} &= \frac{\delta(m_0/q_0)}{m_0/q_0} + \gamma_0^2 \frac{\delta(T_1/T_0)}{T_1/T_0} + k \frac{\delta\beta_1}{\beta_1}, \\ k &= -\frac{\beta_1^2}{1-\beta_1^2} + \left(\frac{T_1}{T_0}\right)^2 \frac{\beta_1^2}{1-(T_1/T_0)^2\beta_1^2}.\end{aligned}\tag{5}$$

The mass of the nucleus of interest is determined with a precision of 10^{-6} when $T_{0,1}$ and β_1 are known to a precision of 10^{-6} and 10^{-4} , respectively. The coefficient k is on the order of 10^{-2} for $\Delta(m/q)/(m_0/q_0)$ of 10^{-2} .

m_1/q_1 can as well be obtained by using the revolution time T_1 corrected by $B\rho$:

$$\begin{aligned}\frac{m_1}{q_1} &= \frac{m_0}{q_0} \frac{T_1}{T_0} \frac{\gamma_0}{\gamma_1} \\ &= \frac{m_0}{q_0} \frac{T_1}{T_0} \sqrt{1 + \frac{1 - (T_0/T_1)^2}{\left(\frac{(m_0/q_0)}{B\rho}c\right)^2}} \\ &= \frac{m_0}{q_0} \frac{T_1''}{T_0}.\end{aligned}\tag{6}$$

T_1'' is the magnetic-rigidity correction to T_1 . In this case, the relative differential of m_1/q_1 is given as:

$$\frac{\delta(m_1/q_1)}{m_1/q_1} = \kappa \frac{\delta(m_0/q_0)}{m_0/q_0} + \lambda \frac{\delta(T_1/T_0)}{T_1/T_0} + \mu \frac{\delta B\rho}{B\rho}.\tag{7}$$

Here, κ , λ , and μ are given as follows:

$$\begin{aligned}\kappa &= \frac{\{(m_0/q_0) c\}^2}{\{(m_0/q_0) c\}^2 + (B\rho)^2 \{1 - (T_0/T_1)^2\}}, \\ \lambda &= \frac{\{(m_0/q_0) c\}^2 + (B\rho)^2}{\{(m_0/q_0) c\}^2 + (B\rho)^2 \{1 - (T_0/T_1)^2\}}, \\ \mu &= \frac{(B\rho)^2 \{1 - (T_0/T_1)^2\}}{\{(m_0/q_0) c\}^2 + (B\rho)^2 \{1 - (T_0/T_1)^2\}}.\end{aligned}\tag{8}$$

The coefficients κ , λ , and μ are on the order of 1, 1, and 10^{-2} , respectively. Thus, the mass of the nucleus of interest is determined with a precision of 10^{-6} when $T_{0,1}$, and $B\rho$ are determined to a precision of 10^{-6} and 10^{-4} , respectively. In the Rare-RI Ring, m_1/q_1 is determined by measuring the revolution times T_0 and T_1 corrected by β_1 or $B\rho$.

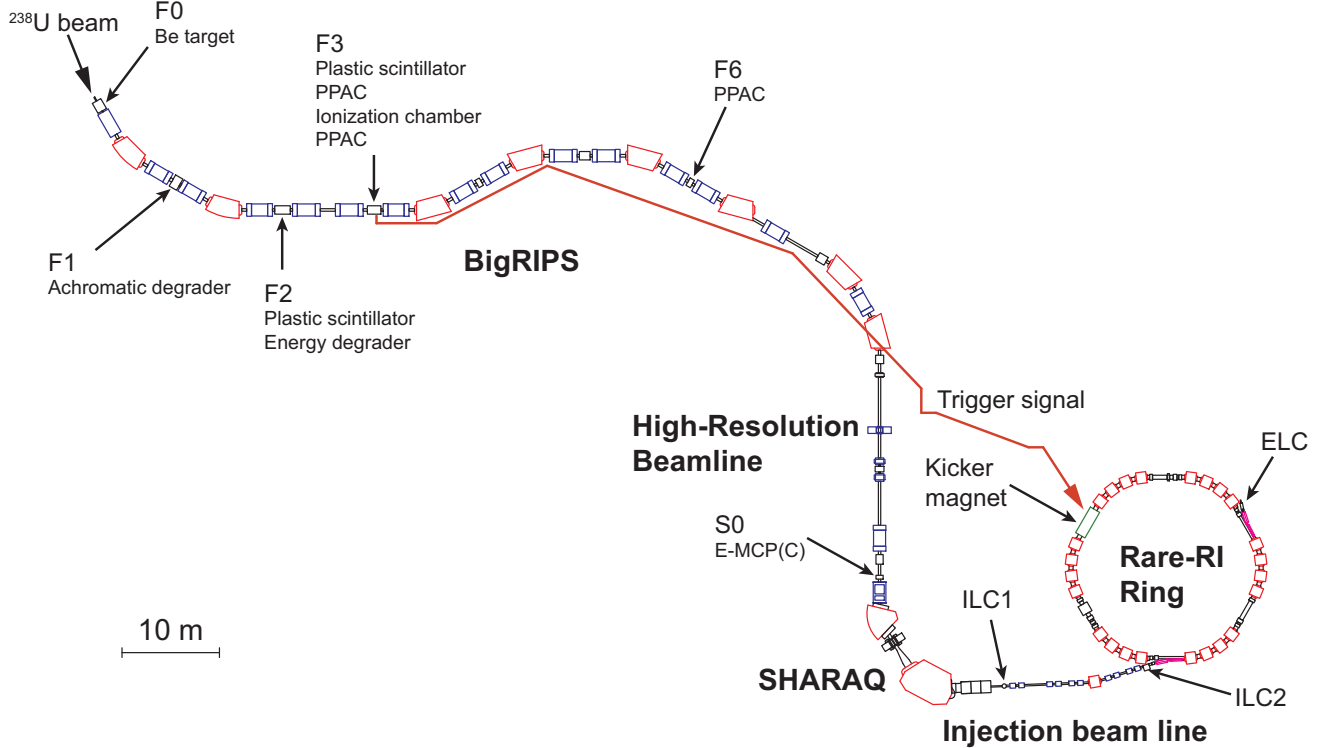


FIG. 1. Layout of the beamlines and the Rare-RI Ring at RIBF. The Rare-RI Ring is located downstream of the SHARAQ spectrometer. The red arrow indicates the path of the trigger signals utilizing the high-speed coaxial tube. Detectors placed in the long-injection beamline are indicated. The E-MCP(C) [48] is a time-of-flight detector equipped with a carbon foil.

III. THE RARE-RI RING FACILITY

A schematic layout of the Rare-RI Ring and the detector configuration used in the discussed experiment are shown in Figs. 1 and 2. The Rare-RI Ring is placed downstream of a long-injection beamline starting from the production target at F0 and consisting of the high-acceptance multi-stage fragment separator BigRIPS [45], the high-resolution beamline [46], the SHARAQ spectrometer [46, 47], and the injection beam line of the Rare-RI Ring itself. The long-injection beamline is mandatory to achieve the individual-ion injection [42] simultaneously with its precise β measurement at 10^{-4} resolution.

The Rare-RI Ring consists of six sectors, each of which has four dipole magnets. To achieve the isochronous ion optical setting, two dipole magnets on both ends of each sector are equipped with ten independent single-turn trim coils. Isochronism on the order of 10^{-6} can be achieved by adjusting the currents in the trim coils.

Because the Rare-RI Ring is coupled to a cyclotron, the injection of a quasicontinuous beam from a cyclotron into the ring is not compatible. A particle-by-particle injection method into the ring, the so-called individual-ion injection method [42], was established. For its realization, a fast response kicker system [49] was developed. The trigger signal for the kicker system is generated by an ion of interest in the plastic scintillator at the focal plane F3; see Fig. 1. To excite the kicker magnets before the arrival of the ion, the signal is transferred to the kicker system using a high-speed coaxial tube [50]. The achieved signal propagation speed was 98.6% of the speed of light. Then, a thyatron switch promptly excites the kicker magnets. We adopted traveling-wave-type kicker magnets to generate a high magnetic field amplitude with a short rise time.

The momentum acceptance of the Rare-RI Ring is designed to be $\pm 0.5\%$. The transverse acceptances are 150π and 30π mm mrad in the horizontal and vertical planes, respectively. The residual gas pressure in the Rare-RI Ring ranges from 2.5×10^{-6} to 4.0×10^{-5} Pa achieved without baking. Although the pressure is not at ultrahigh vacuum level, it is sufficient to store particles for approximately 2000 turns.

IV. FIRST DEMONSTRATION OF MASS MEASUREMENT

The first mass measurement of exotic nuclei was performed on five fully stripped nuclei, namely ^{79}As , ^{78}Ge , ^{77}Ga , ^{76}Zn , and ^{75}Cu , all of which have well-known masses tabulated in the Atomic Mass Evaluation, AME2020 [53]. ^{78}Ge was chosen to be the reference particle for tuning the beam transport and isochronous ion optics of the ring. The masses, revolution times, and time-of-flights (TOFs) between F3 and S0 of ^{79}As , ^{78}Ge , ^{77}Ga , and ^{76}Zn were used to fix the parameters for the velocity β and magnetic rigidity $B\rho$ determination, which is further detailed below. Subsequently, the mass of ^{75}Cu was obtained relative to the mass and revolution time of ^{78}Ge .

The procedure for determining the mass at the Rare-RI Ring is divided into the following five steps: (1) production of RIs; (2) injection of RIs into the ring; (3) circulation confirmation of RIs in the ring; (4) fine-tuning of the isochronous optical setting; (5) storage for several thousands of turns and extraction of RIs. The timing signals at the injection and extraction provide the total TOF.

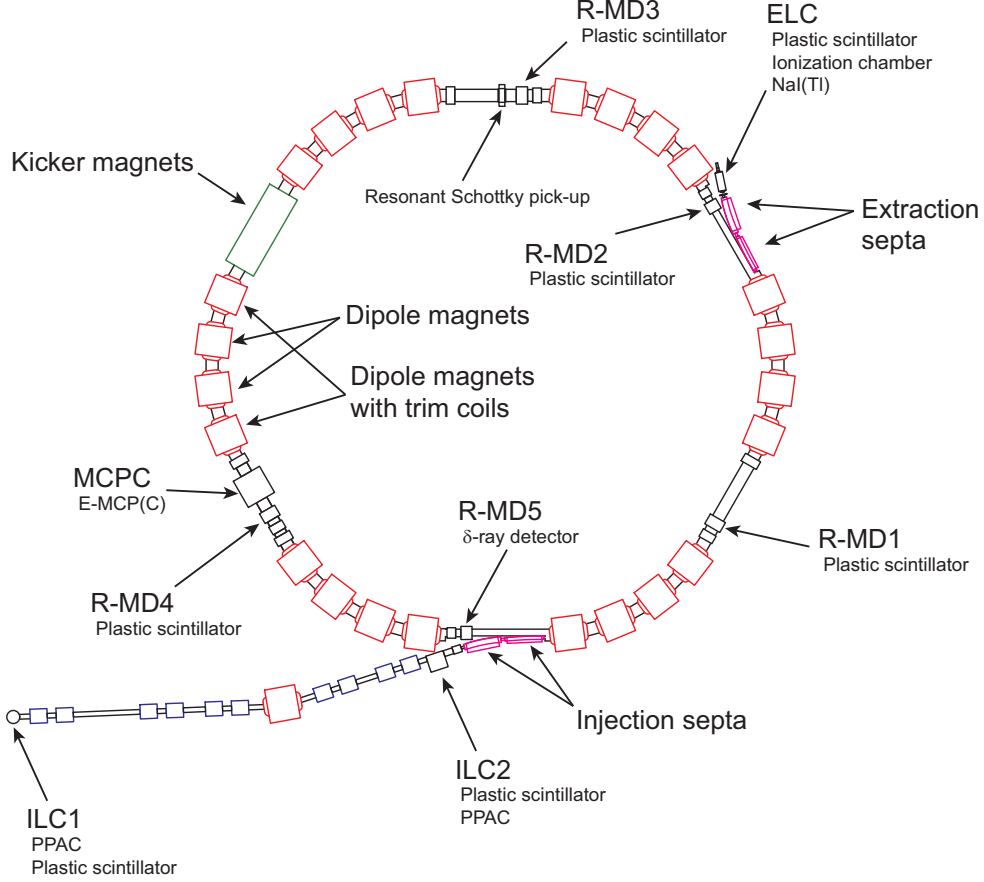


FIG. 2. Structure of the Rare-RI Ring with the detector setup. Plastic scintillators placed at R-MD1, R-MD2, and R-MD3 were used to determine the trajectories of the injected ions. A plastic scintillator at R-MD4 was used to verify synchronization of the kicker timing with the particle arrival and the kicking angle. The E-MCP(C) [48] and δ -ray detector [51] were utilized to confirm the storage of particles. A resonant Schottky pickup [52] was installed for precise tuning of the isochronous optics by using long-lived species. For particle identification, an ionization chamber and a NaI(Tl) counter were set up at the ring ejection channel ELC to measure the energy loss and total energy, respectively.

A. RIs production and events selection

Exotic nuclei near ^{78}Ge were produced via in-flight fission of ^{238}U beams impinging at an energy of 345 MeV/nucleon on a 10-mm-thick ^9Be target. Fission fragments have a large momentum spread of several percent and only a small fraction of them could be transported and injected into the ring. By considering an additional momentum-broadening effect in

degraders and detectors mounted in BigRIPS, a momentum slit at the dispersive focal plane F1 of the BigRIPS was set to ± 2 mm, corresponding to $\pm 0.09\%$ in momentum.

Standard particle separation was achieved by a combined analysis of the magnetic rigidity and energy loss in the degraders. In this experiment, the magnetic rigidity of the BigRIPS was adjusted to enhance the purity of ^{78}Ge , which was approximately 40% at F3. A wedge-shaped achromatic degrader made of 5-mm-thick aluminum was inserted at F1. A slit with a ± 2 mm opening at the achromatic focal plane F2 was used to remove undesired contaminants. An additional energy degrader made of 5.6-mm-thick aluminum placed at F2 was used for fine tuning the energy of the fragments. The beam energy of ^{78}Ge at F3 was approximately 175 MeV/nucleon.

The energy deposit ΔE in the ionization chamber at F3 and the TOF between F2 and F3 were measured for particle identification. A typical particle-identification plot is presented in Fig. 3. All the nuclei which generate the trigger signal are indicated by the green dots. To select the valid events, a Gaussian fitting was applied to the ΔE and TOF spectra. In this analysis, the selection gates of ± 2.6 standard deviations were applied for both the ΔE and TOF spectra, as indicated by the blue symbols in Fig. 3.

B. Injection of RIs into the ring

The fission fragments identified at F3 were transported to the ring via the long-injection beamline. Several detectors were placed along it for beam diagnostics. The momenta of the nuclei of interest were measured at the dispersive focal plane F6 of the BigRIPS by using a position-sensitive parallel-plate avalanche counter (PPAC) [54]. The momentum dispersion at F6 (D_{F6}) was measured in this experiment to be 72.5(6) mm/%.

Afterwards, the fission fragments passed through the septum magnets and arrived at the kicker magnets. After the accomplishment of the beam tuning, the detectors placed in the long-injection beamline were removed, except for those placed at F2, F3, F6, and S0. The fission fragments were then individually injected into the ring utilizing the fast-response kicker system [49]. The flight time of the ions from F3 to the kicker was approximately 1 μs . The magnetic field of the kicker reached a flat top 950 ns after the trigger signal was generated at F3. This includes the time delays needed for the signal propagation from F3 to the kicker, internal kicker electronic processing, and the response of the magnet itself. To

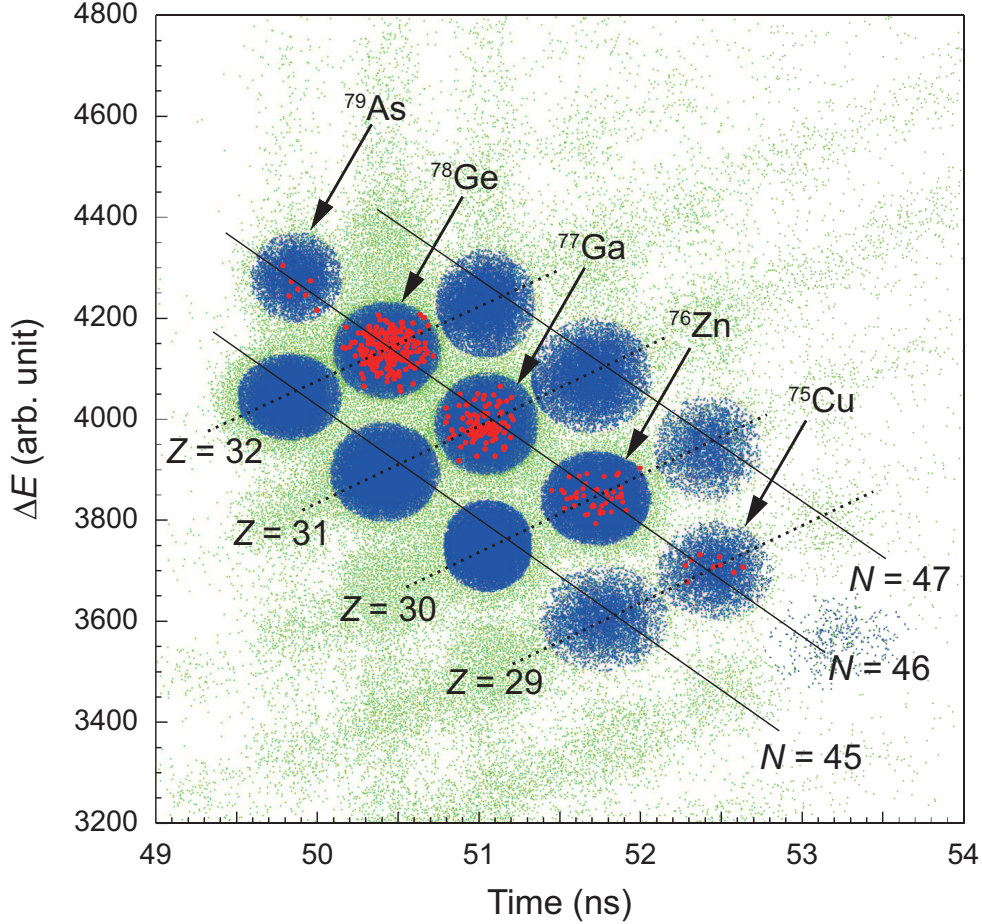


FIG. 3. Particle identification plot. The vertical and horizontal axes represent the energy deposit in the ionization chamber and the TOF between F2 and F3, respectively. The green, blue, and red dots indicate all ions causing valid trigger events, namely the particles identified and selected at F3, and the ions injected, stored, extracted from the ring and selected at ELC, respectively.

synchronize the particle arrival and the excitation of the magnetic field, an additional 50 ns delay was implemented. A typical waveform of the kicker magnetic field and a histogram of arrival times of the ions of interest at R-MD4 are shown in Fig. 4. As a result, the entire range of the ions of interest could be injected in a single optimized timing setting.

C. Confirmation of circulation of RIs

Since only a single ion is injected at a time, standard beam diagnostics is insufficiently sensitive. The first challenge is to control whether an injected particle is revolving in the ring. The circulation of the stored particles was confirmed using an in-ring TOF detector,

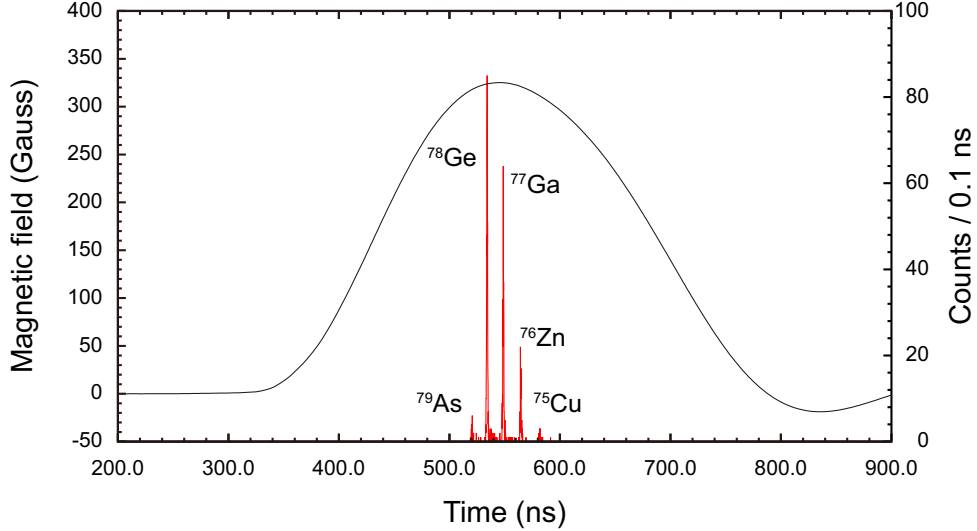


FIG. 4. Waveform of the kicker magnetic field and a histogram of the arrival times of particles of interest. Only the successfully injected particles are considered. The zero of the time scale corresponds to the time when the trigger signal arrived at the kicker, that is the time at F3 with a constant offset of about $1 \mu\text{s}$. The left and right vertical axes are the magnetic field and counting rates per 0.1 ns, respectively.

termed E-MCP, equipped with a carbon foil [E-MCP(C)] [48] placed at MCPC; see Fig. 2. The obtained time spectra of ^{78}Ge , ^{77}Ga , and ^{76}Zn are shown in Fig. 5. The observed periodic time signals indicate that particle circulation was successfully achieved. Stored ^{78}Ge ions circulated for about 60 turns.

The corresponding revolution times were obtained through the analysis described in detail in Ref. [48]. The results are presented in Table I. The amounts of ^{79}As and ^{75}Cu were insufficient for deducing their revolution times directly. Nevertheless, the revolution times for ^{79}As and ^{75}Cu can be deduced using Eq. (3) and ^{78}Ge as reference. In this analysis, the β values of ^{79}As , ^{75}Cu , and ^{78}Ge can be calculated by taking the magnetic rigidity of $B\rho = 4.8513 \text{ Tm}$ as measured by an NMR probe located in the ring. The calculated revolution times for ^{79}As and ^{75}Cu are also presented in Table I. After the circulation of the ions in the ring was confirmed, the destructive E-MCP(C) was removed from the ring aperture.

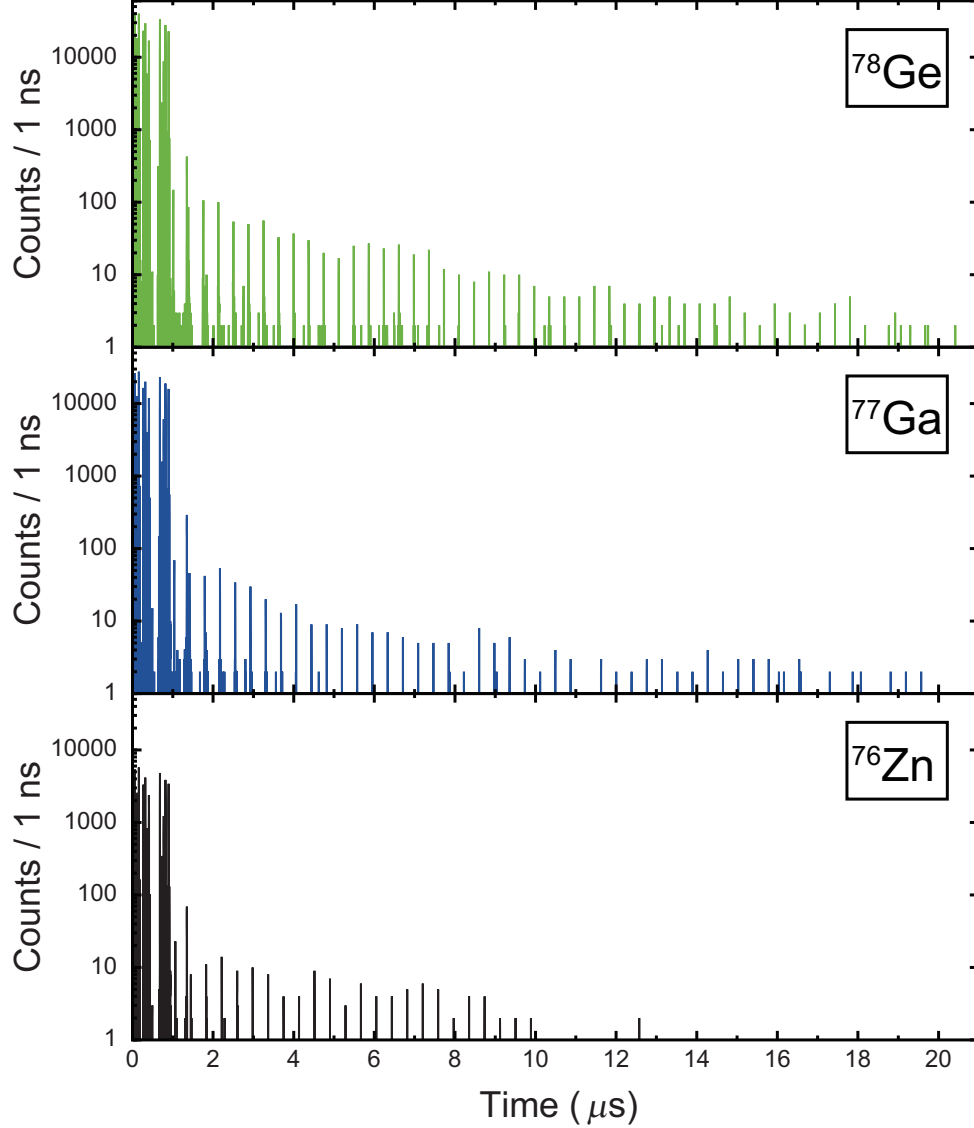


FIG. 5. Time signals of ^{78}Ge , ^{77}Ga , and ^{76}Zn taken from Ref. [48]. Noise at 0–1 μs is due to the kicker magnets.

D. Fine-tuning of the isochronous ion optics

The quality of the isochronous ion optics is decisive for mass determination in isochronous mass spectrometry. The optics is extremely sensitive to the applied magnetic fields and their quality. The currents of the trim coils incorporated into the dipole magnets of the ring were tuned to obtain the required magnetic-field distribution. The magnetic field setting was optimized for the reference particle, ^{78}Ge , by monitoring the correlation between the TOF from S0 to ELC ($\text{TOF}_{\text{S0ELC}}$) and the particle momentum, which was measured at F6 prior to

TABLE I. Measured and calculated revolution times of stored ions. See text for more details.

RI	Measured revolution time (ns)	Calculated revolution time (ns)
^{79}As		368.404
^{78}Ge	373.121(2)	
^{77}Ga	378.192(3)	
^{76}Zn	383.615(5)	
^{75}Cu		389.448

the injection into the ring. If isochronous ion optics is perfectly optimized for the reference particle ^{78}Ge , the $\text{TOF}_{\text{S0ELC}}(^{78}\text{Ge})$ will be constant and independent of momentum. Thus, the quality of the isochronous ion optics is quantified by the momentum dependence on $\text{TOF}_{\text{S0ELC}}(^{78}\text{Ge})$. In this experiment, second-order ion-optical tuning was adopted.

Green symbols in Fig. 6 demonstrate the momentum dependence of the $\text{TOF}_{\text{S0ELC}}$ of ^{78}Ge reference particles. In this figure, the abscissa axis is the momentum (p) deviation from the momentum at a weighted average position at F6 (p_0), $dp/p_0 = (p - p_0)/p_0$. The momentum deviation was calculated using the position information of the events at F6 (P_{F6}), the weighted average of P_{F6} (P_{F6avg}) described in Sec. V B, and the momentum dispersion at F6 (D_{F6}) as $dp/p_0 = (P_{\text{F6}} - P_{\text{F6avg}})/D_{\text{F6}}$. The E-MCP(C) at S0 and the plastic scintillator at ELC were used to measure $\text{TOF}_{\text{S0ELC}}$. Owing to the second-order tuning of the magnetic fields, a small third-order dependence appeared in the correlation between $\text{TOF}_{\text{S0ELC}}(^{78}\text{Ge})$ and the momentum. A precision of $\text{TOF}_{\text{S0ELC}}(^{78}\text{Ge})$ was achieved to be 4.7 ppm (standard deviation) for a momentum spread of $\pm 0.3\%$.

E. Storage and extraction of RIs and TOF measurement

After a defined storage time, the particles were extracted from the ring using the same kicker magnets and the same magnetic field distribution as the one used for the injection. Two storage-time intervals were set, namely 700.6 μs to extract ^{79}As , ^{78}Ge , ^{77}Ga , and ^{75}Cu , and 700.4 μs for ^{76}Zn .

Total flight time $\text{TOF}_{\text{S0ELC}}$ spectra are shown in Fig. 6. In contrast to the $\text{TOF}_{\text{S0ELC}}$ of ^{78}Ge , momentum dependences are clearly observed in $\text{TOF}_{\text{S0ELC}}$ for ^{79}As , ^{77}Ga , ^{76}Zn , and

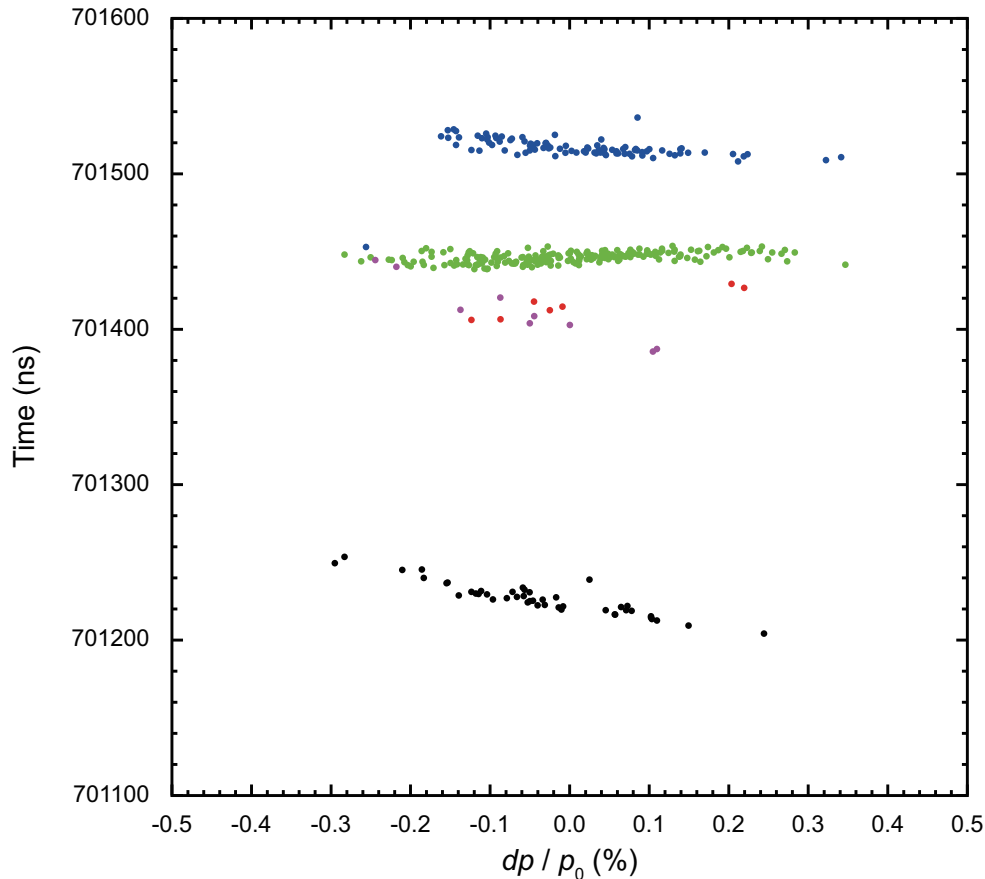


FIG. 6. Momentum dependence of the total flight time $\text{TOF}_{\text{S0ELC}}$. The red, green, blue, black, and purple circles indicate ^{79}As , ^{78}Ge , ^{77}Ga , ^{76}Zn , and ^{75}Cu , respectively.

^{75}Cu . The $\text{TOF}_{\text{S0ELC}}$ of approximately 0.7 ms was used instead of measuring revolution times in the ring turn by turn. The latter would be advantageous, but the corresponding detector needs to be non-destructive, which remains a challenge. The previously discussed E-MCP(C) counter introduces energy losses in the carbon foil, which limits the particle storage to only a few tens of turns, whereas about 2000 revolutions are needed to achieve the anticipated mass precision.

The number of turns for each particle was determined using the revolution time and the time interval between injection and extraction. The obtained turn numbers N are listed in Table II. In the mass determination, the listed turn numbers were incremented by 2 in consideration that the sum of the flight path lengths from S0 to the kicker and from the kicker to ELC is approximately twice the ring circumference.

A long-range time-to-digital converter (Acqiris TC842 [55]) was used to measure the total

TOF_{S0ELC} defined by the start signal from the E-MCP(C) at S0 and the stop signal from the plastic scintillator at ELC. The signals from the E-MCP(C), plastic scintillator, and the trigger detector were processed through a constant fraction discrimination (Ortec935 [56]) before being fed into the Acqiris TC842.

TABLE II. Numbers of turns, N , of stored ^{79}As , ^{78}Ge , ^{77}Ga , ^{76}Zn , and ^{75}Cu . See text for more details.

RI	Number of turns N
^{79}As	1902
^{78}Ge	1878
^{77}Ga	1853
^{76}Zn	1826
^{75}Cu	1799

V. MASS DETERMINATION

To determine m_1/q_1 using Eqs. (4) and (6), the revolution times $T_{0,1}$ and the velocity β_1 or magnetic rigidity $B\rho$ need to be known. The revolution times $T_{0,1}$ were calculated using the corresponding TOF_{S0ELC} and N . Since T_1 can be corrected by using either β_1 or $B\rho$, there are two analytical methods for determining m_1/q_1 .

A. Extracted events selection

As described in Sec. IV A, the fission fragments were identified at F3 prior to injection. Furthermore, the fragments were also identified at ELC as successfully extracted events. The extracted events were defined as those that had proper TOF stop data from the plastic scintillator at ELC. In addition, events were selected from a particle identification at ELC using the total energy E and ΔE information obtained by the NaI(Tl) counter and ionization chamber, respectively, as shown in Fig 7. The selection gates of ± 3.0 and ± 1.5 standard deviations were applied to both the E and ΔE spectra, respectively. The selected valid extraction events obtained in a 3-hour-accumulation period are plotted and indicated by the

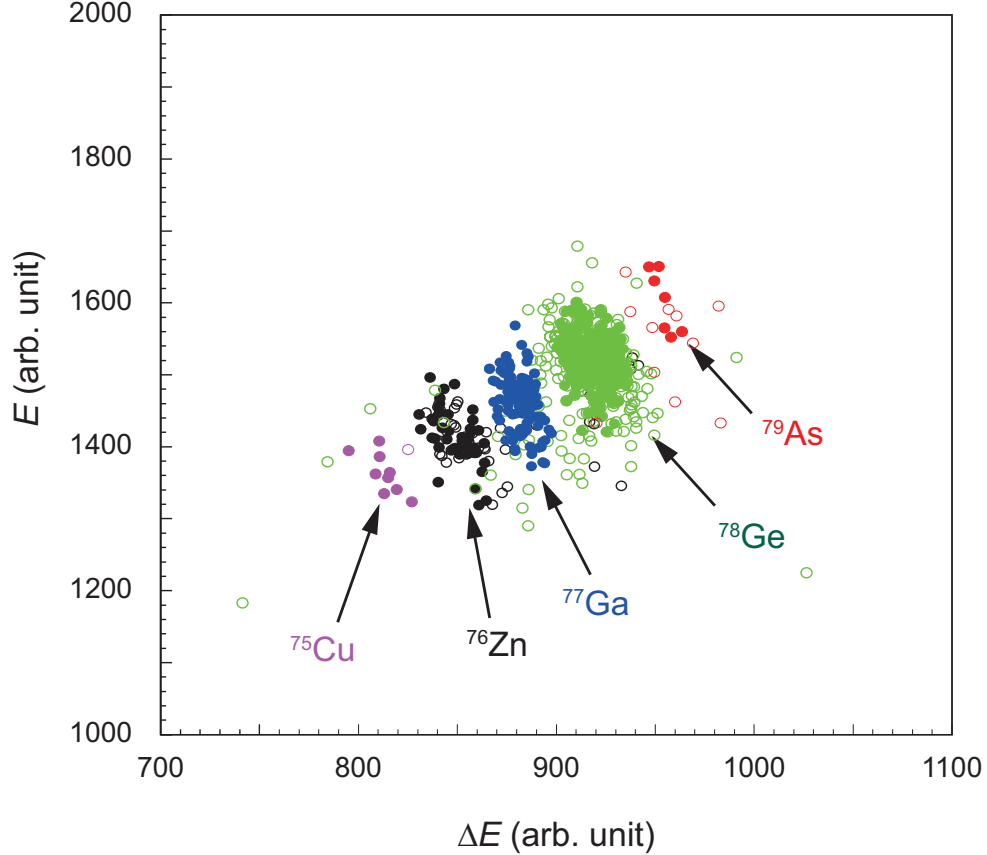


FIG. 7. Particle identification plot at ELC. The open and filled circles indicate the events selected at F3 and the events selected at ELC, respectively.

red dots in Fig. 3. The number of selected extraction events is listed in Table III.

B. Velocity determination

Absolute values of velocity β are crucial for correcting T_1 via Eq. (4). Each β value was calculated employing TOF from F3 to S0, TOF_{F3S0} , as:

$$\beta = \frac{L_{\text{F3S0}}}{c(\text{TOF}_{\text{F3S0}} + O)}, \quad (9)$$

where L_{F3S0} is the flight path length between F3 and S0, and O is the offset of the measured TOF_{F3S0} . To obtain L_{F3S0} and O , we assume that the velocities between F3 and S0, v_{F3S0} ,

TABLE III. Numbers of extracted events of ^{79}As , ^{78}Ge , ^{77}Ga , ^{76}Zn , and ^{75}Cu . See text for more details.

RI	Number of events
^{79}As	7
^{78}Ge	218
^{77}Ga	94
^{76}Zn	45
^{75}Cu	9

and between S0 and ELC, v_{S0ELC} , are the same. Thus, the following equations hold:

$$\begin{aligned} \frac{L_{\text{F3S0}}}{\text{TOF}_{\text{F3S0}} + O} &= \frac{L_{\text{ring}}}{T_{0,1}}, \\ \text{TOF}_{\text{F3S0}} &= \frac{L_{\text{F3S0}}}{L_{\text{ring}}} T_{0,1} - O, \end{aligned} \quad (10)$$

where $L_{\text{ring}} = 60.335(2)$ m is the flight length in the ring, see Sec. V C. To obtain the precise velocities, we used momentum-corrected $\text{TOF}_{\text{F3S0-cor}}$ and $T_{0,1-cor}$ instead of TOF_{F3S0} and $T_{0,1}$ in Eq. (10) using the following equations:

$$\begin{aligned} \text{TOF}_{\text{F3S0-cor}} &= \text{TOF}_{\text{F3S0}} - a (P_{\text{F6}} - P_{\text{F6avg}}), \\ T_{0,1-cor} &= T_{0,1} - a' (P_{\text{F6}} - P_{\text{F6avg}}), \end{aligned} \quad (11)$$

where a (a') denotes the slope of the TOF_{F3S0} -position(momentum) ($T_{0,1}$ -position) correlation. The slopes of the correlations were obtained by a fitting analysis using a first-order polynomial. An example of the correlation plot of T_1 for ^{76}Zn is shown by the black filled circles in Fig. 8. The momentum dependence of T_1 is clearly seen and can be corrected accordingly. The corrected T_1 , T_{1-cor} , is indicated by the black open circles in Fig. 8. The momentum dependence was sufficiently reduced through this procedure. The same analysis was performed for ^{79}As , ^{78}Ge , ^{77}Ga , and ^{76}Zn .

Figure 9 depicts the position distributions for each stored nuclear species at the dispersive focal plane F6. The weighted average position, $P_{\text{F6avg}} = 0.04(44)$ mm, is indicated by the blue line in Fig. 9, which was obtained by considering the weighted average of the individual weighted average positions of ^{79}As , ^{78}Ge , ^{77}Ga , and ^{76}Zn .

L_{F3S0} and O were determined through a linear fit according to Eq. (10) of the correlation plot between $\text{TOF}_{\text{F3S0-cor}}$ and $T_{0,1-cor}$, as shown in Fig. 10. The uncertainties of $\text{TOF}_{\text{F3S0-cor}}$

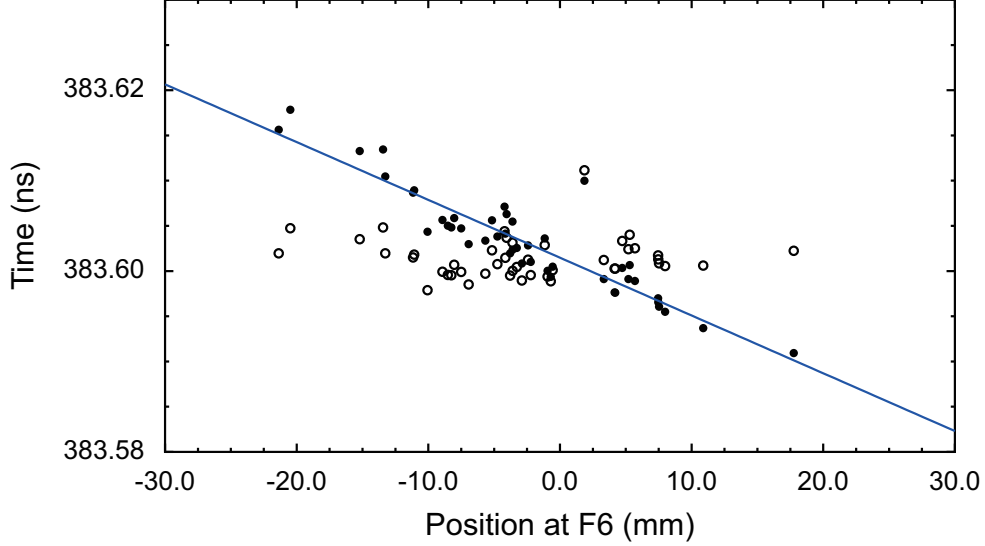


FIG. 8. Correlation between T_1 ($T_{1-\text{cor}}$) and the position at F6 for ^{76}Zn . The black filled circles indicate T_1 and the blue line represents a straight-line fit result. The black open circles indicate $T_{1-\text{cor}}$.

were about 0.3 to 1.6 ps, while the fit residua [$\text{TOF}_{\text{F3S0-cor}}(\text{exp}) - \text{TOF}_{\text{F3S0-cor}}(\text{fit})$] were within ± 10 ps. The resultant L_{F3S0} and O values are $L_{\text{F3S0}} = 84.465(5)$ m and $O = 313.47(2)$ ns. The β values of ^{75}Cu were calculated event-by-event using Eq. (9) adopting the measured TOF_{F3S0} , flight length L_{F3S0} , and offset O .

Based on the principle of mass measurement, $\beta_1 T_1$ of ^{75}Cu should coincide with $\beta_0 T_0$. However, the experimental $\beta_1 T_1$ of ^{75}Cu exhibited a small difference. Possible reasons for this disagreement may be the momentum-dependent flight path lengths and energy losses in the PPAC at F6, which could not be accurately considered. These effects are sources of systematic uncertainties. To account for them, we introduced a correction factor for β_1 of ^{75}Cu to match $\beta_0 T_0$. The correction factor is defined as the ratio $R = \beta_0 T_0 / \beta_1 T_1(^{75}\text{Cu})$ at P_{F6avg} . To obtain the ratio R , the experimental $\beta_0 T_0$ and $\beta_1 T_1(^{75}\text{Cu})$ as a function of the F6 position were fitted using the first-order polynomial, as shown in Fig. 11. The fit results of the βT values at the F6 weighted average position were used to calculate the ratio R giving $R = 1.00023(20)$ for ^{75}Cu . The final β taken for the mass determination was obtained via $\beta_{1-\text{cor}} = R\beta_1$.

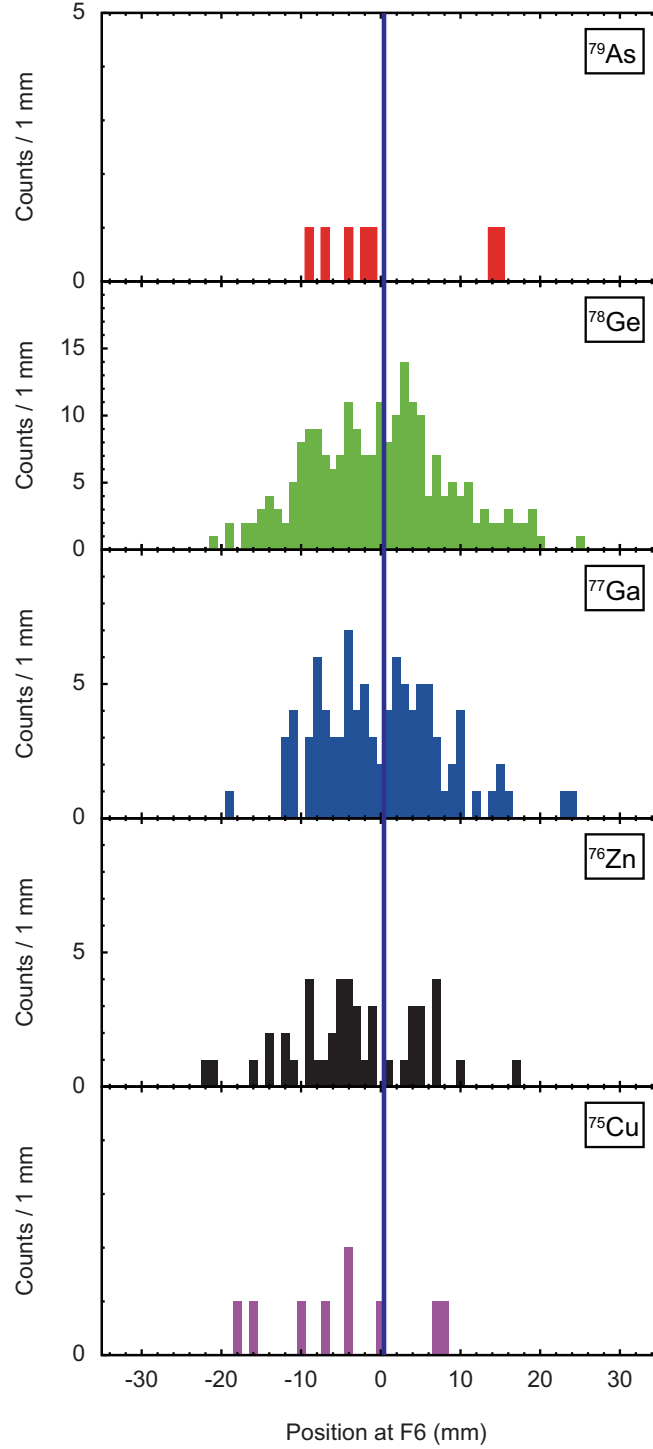


FIG. 9. Position distribution of each isotope at F6. The blue line indicates the weighted average position ($P_{F6\text{avg}}$). See text for more details.

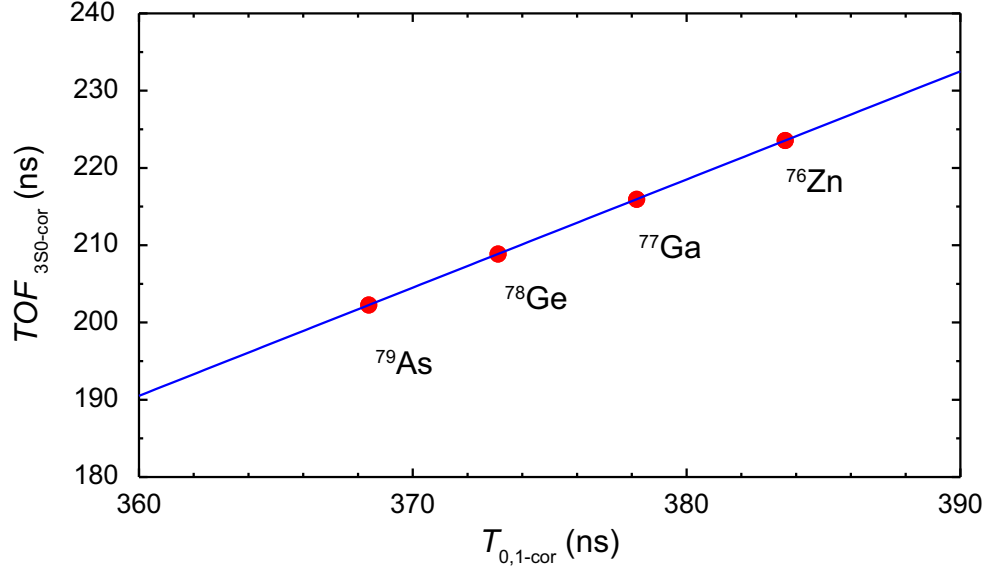


FIG. 10. Relationship between $\text{TOF}_{\text{F3S0-cor}}$ and $T_{0,1\text{-cor}}$. The blue line is a linear fit result. All error bars are smaller than the symbol size.

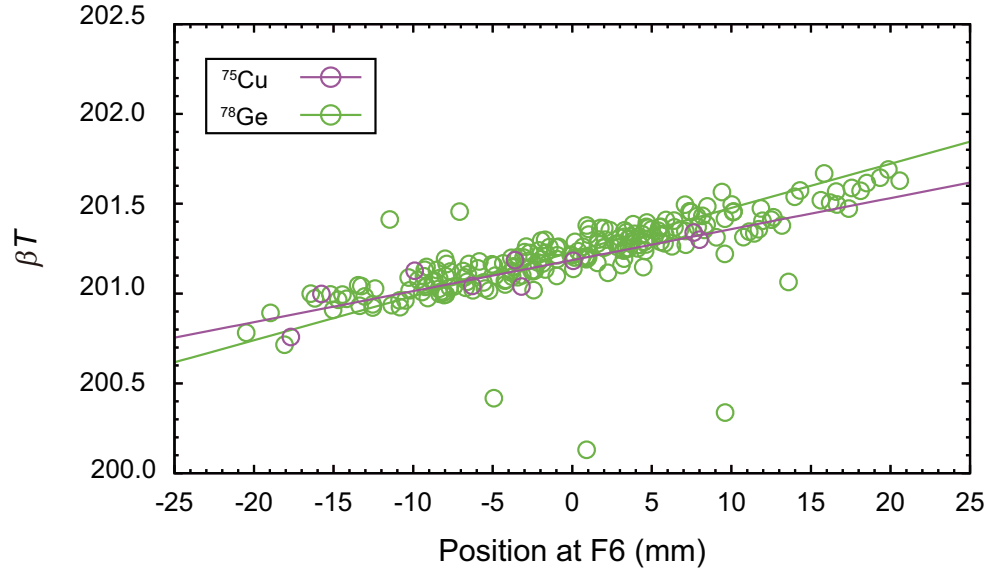


FIG. 11. βT as a function of position at F6 for ^{75}Cu and ^{78}Ge . The solid lines are fit results. See text for more details.

C. Magnetic rigidity determination

The absolute magnetic rigidities of each particle are crucial for correcting T_1 via Eq. (6). The magnetic rigidities were not directly measured for each event and were thus calculated using the following equation:

$$B\rho = B\rho_{\text{ring}} \left\{ 1 + \frac{(P_{\text{F6}} - P_{\text{F6avg}})}{D_{\text{F6}}} \right\}, \quad (12)$$

where $B\rho_{\text{ring}}$ is the mean value of the magnetic rigidity of the ring, P_{F6} is the F6 position, P_{F6avg} is the weighted average position at F6, and $D_{\text{F6}} = 72.5(6)$ mm/% is the dispersion measured at F6.

Based on the definition of magnetic rigidity, the relationship between m/q (u/q) and $B\rho$ is:

$$\frac{m}{q} = \frac{B\rho}{\gamma v} = \frac{B\rho\sqrt{1 - (v/c)^2}}{v}, \quad (13)$$

where u and v denote the unified atomic mass unit, and velocity, respectively. The velocity, respectively can be expressed as l/t with a flight length l and time-of-flight t . Hence, the relationship between t and $B\rho$ is obtained:

$$t^2 = \left(\frac{l}{B\rho} \right)^2 \left(\frac{m}{q} \right)^2 + \left(\frac{l}{c} \right)^2. \quad (14)$$

To evaluate $B\rho_{\text{ring}}$, the momentum-corrected revolution times $T_{0,1-\text{cor}}$ and the mean ring circumference L_{ring} are taken as t and l , respectively, in Eq. (14). Figure 12 presents t^2 as a function of the squared mass-to-charge ratio $(m/q)^2$ from AME2020 [53]. A linear fitting analysis using Eq. (14) provided $B\rho = B\rho_{\text{ring}}$ and $l = L_{\text{ring}}$ as free parameters. Consequently, $B\rho_{\text{ring}}$ and L_{ring} were obtained to be $B\rho_{\text{ring}} = 4.8457(2)$ Tm and $L_{\text{ring}} = 60.335(2)$ m. Whereas the uncertainties of the t^2 data points are about 0.1 to 0.3 ns², the corresponding uncertainties of the fit residua [$t^2(\text{exp}) - t^2(\text{fit})$] are as small as ± 0.1 ns². The obtained magnetic field in the analysis was different from that measured by the NMR probe in the ring described in Sec. IV C. This difference could be attributed to the fact that the NMR probe in the ring was not installed at a position corresponding to the momentum at P_{F6avg} . The magnetic rigidities of each particle were determined through Eq. (12).

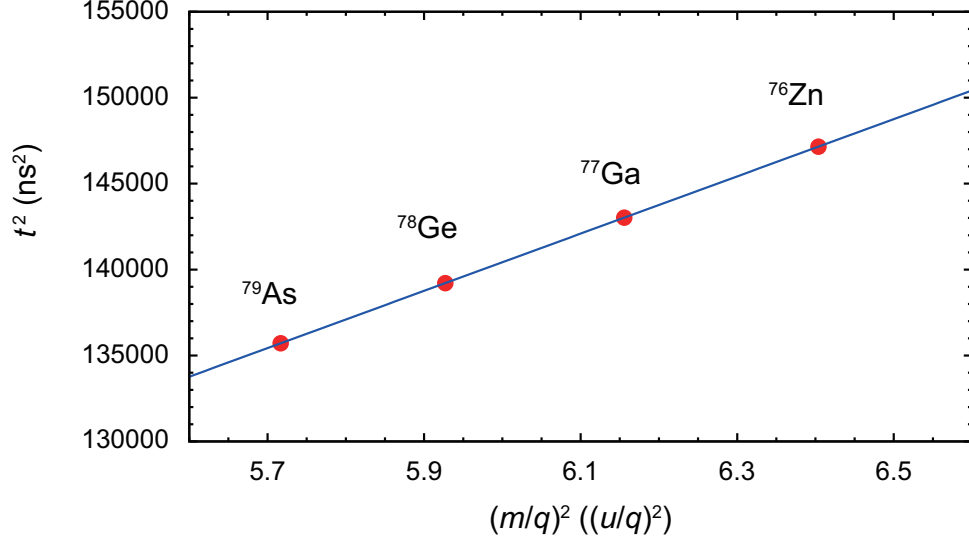


FIG. 12. Relationship between t^2 and $(m/q)^2$ according to Eq. (14). The blue line indicates the result of the fitting analysis. The error bars of t^2 are smaller than the symbol size.

D. Revolution times in the Rare-RI Ring

The revolution times $T_{0,1} = \text{TOF}_{\text{S0ELC}}/(N + 2)$ obtained for ⁷⁸Ge and ⁷⁵Cu are shown in Fig. 13 as a function of the momentum measured at F6. Because isochronism is fulfilled for the reference ⁷⁸Ge, the momentum dependence of T_0 of ⁷⁸Ge is not observed; however, that of ⁷⁵Cu is apparent and can be corrected using β or $B\rho$. Figure 13 (bottom) presents T_1'' , which is corrected by $B\rho$. The mean T_0 value was 373.1098(1) ns, and the mean T_1'' value was 395.961(1) ns. Therefore, the uncertainty of T_0 is on the order of 10^{-7} and that of T_1'' is on the order of 10^{-6} . The uncertainty of T_0 mainly stems from the magnetic field instabilities and time resolutions of the timing detectors at S0 and ELC.

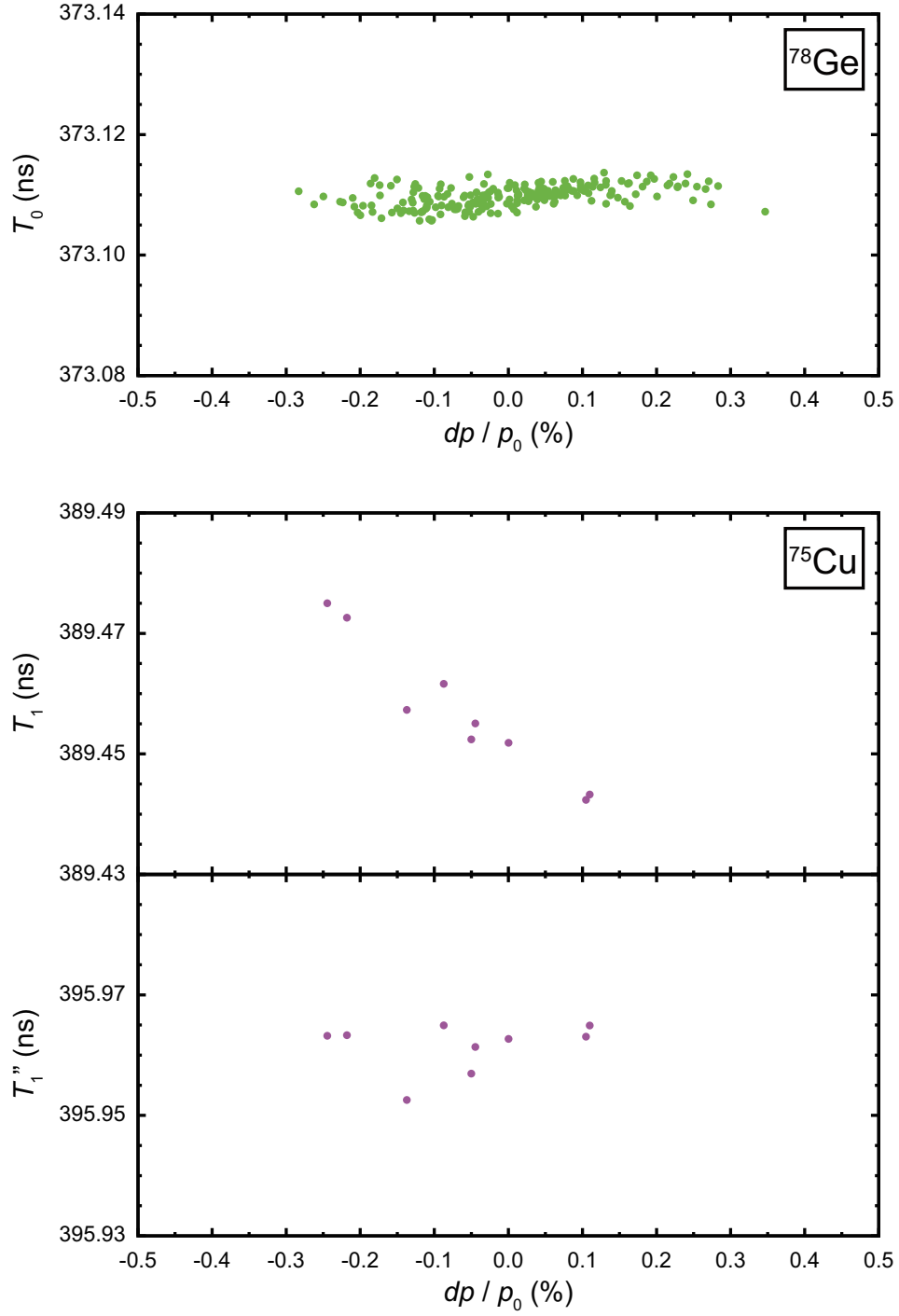


FIG. 13. Top and middle: Relationship between $T_{0,1}$ as a function of the momentum. Bottom: $B\rho$ corrected T_1'' of ^{75}Cu .

E. Masses

The m_1/q_1 values were evaluated for each event by adopting the corresponding T_1 , β , and $B\rho$ in Eqs. (4) and (6). In the analyses, a constant T_0 value of 373.1098 ns was used. Because the mass of ^{75}Cu is well known, comparing the obtained experimental values to the literature values from AME2020 [53] allows the verification of the present mass determination procedure. Figure 14 presents the m_1/q_1 spectra of ^{75}Cu obtained using the β and $B\rho$ corrections. The m_1/q_1 value $m_1/q_1(\beta) = 2.583644(27)$ u/ q was obtained by employing the β correction and $m_1/q_1(B\rho) = 2.583650(11)$ u/ q by employing the $B\rho$ correction. Figure 15 presents a comparison of the experimental m_1/q_1 values with the literature m/q value [$m_1/q_1(\text{AME2020}) = 2.58364357(3)$ u/ q]. The differences between the experimental and literature values is less than 1×10^{-5} u/ q . The mass excess (ME) values obtained in these measurements are $ME(\beta) = -54460(740)$ keV and $ME(B\rho) = -54310(290)$ keV, while the literature mass excess value is $ME(\text{AME2020}) = -54470.2(7)$ keV [53].

The total uncertainty for the β correction analysis was deduced via

$$\delta\left(\frac{m_1}{q_1}\right)_\beta = \sqrt{\left(\delta\frac{m_1}{q_1}\right)_{\text{sta}}^2 + \left(\delta\frac{m_1}{q_1}\right)_{T_0}^2 + \left(\delta\frac{m_1}{q_1}\right)_{\beta_1}^2 + \left(\delta\frac{m_1}{q_1}\right)_R^2}, \quad (15)$$

where $\delta(m_1/q_1)_{\text{sta}}$ is the statistical uncertainty of m_1/q_1 , and $\delta(m_1/q_1)_{T_0}$, $\delta(m_1/q_1)_{\beta_1}$, and $\delta(m_1/q_1)_R$ are propagated statistical uncertainties from T_0 , β_1 , and R corrections, respectively. For the $B\rho$ correction analysis, the total uncertainty is given as

$$\delta\left(\frac{m_1}{q_1}\right)_{B\rho} = \sqrt{\left(\delta\frac{m_1}{q_1}\right)_{\text{sta}}^2 + \left(\delta\frac{m_1}{q_1}\right)_{T_0}^2 + \left(\delta\frac{m_1}{q_1}\right)_{B\rho_{\text{ring}}}^2 + \left(\delta\frac{m_1}{q_1}\right)_{D_{F6}}^2 + \left(\delta\frac{m_1}{q_1}\right)_{P_{F6\text{avg}}}^2}, \quad (16)$$

where $\delta(m_1/q_1)_{B\rho_{\text{ring}}}$, $\delta(m_1/q_1)_{D_{F6}}$, and $\delta(m_1/q_1)_{P_{F6\text{avg}}}$ are the uncertainties due to the error propagation from $B\rho_{\text{ring}}$, D_{F6} , and $P_{F6\text{avg}}$, respectively. Because the relative uncertainty of $\delta(m_0/q_0)/(m_0/q_0)$ is negligible ($\approx 3 \times 10^{-8}$), we neglected this contribution in the analyses.

The statistical uncertainties of m_1/q_1 values were obtained using the standard deviation, σ , of the m_1/q_1 distribution and the number of events, n , using the equation $\delta(m_1/q_1)_{\text{sta}} = \sigma/\sqrt{n}$. These uncertainties were deduced to be $\delta(m_1/q_1)_{\text{sta}}(\beta) = 1.3 \times 10^{-5}$ u/ q and $\delta(m_1/q_1)_{\text{sta}}(B\rho) = 8.9 \times 10^{-6}$ u/ q for the β and $B\rho$ corrections, respectively. The time fluctuations of the ring magnetic field change the time-of-flight in the ring and broaden the peak width of the m/q spectrum. As a result, it affects the statistical uncertainty of m_1/q_1 .

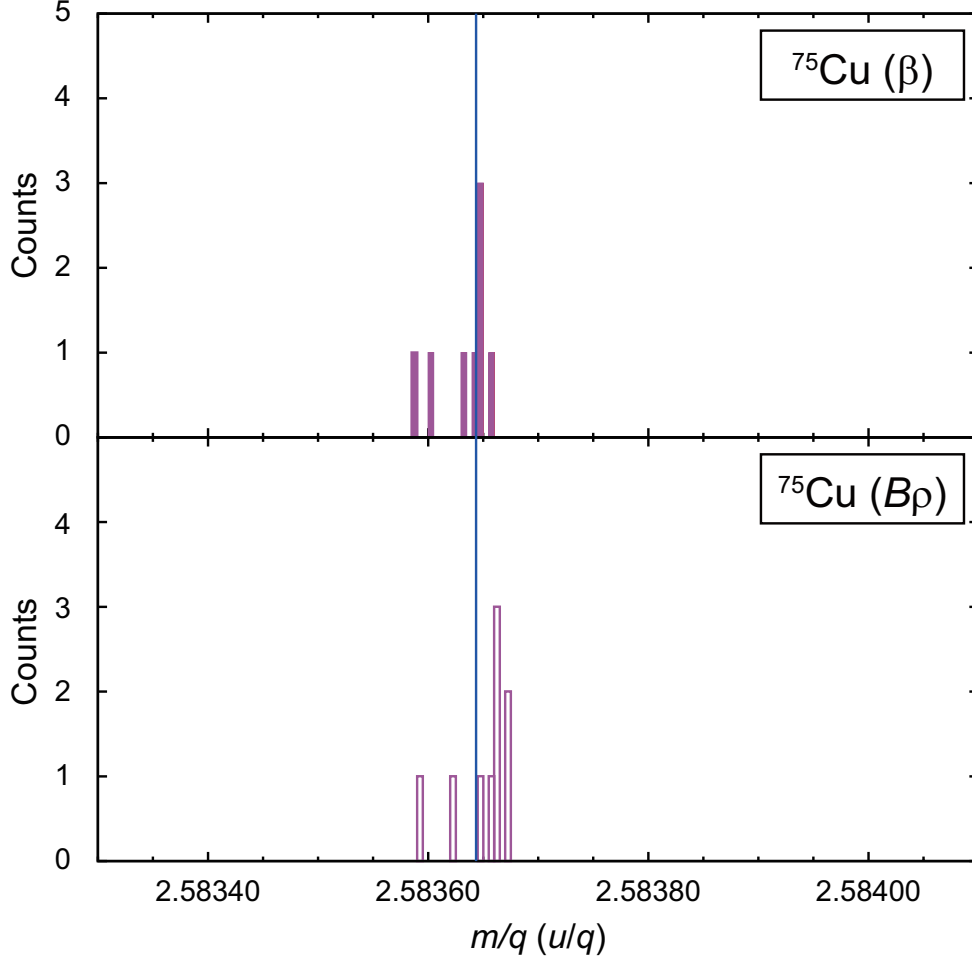


FIG. 14. m_1/q_1 spectra of ^{75}Cu obtained adopting the β and $B\rho$ corrections. The blue line indicates the literature value.

Figure 16 (a) presents the typical time fluctuations of the magnetic field of a dipole magnet during the measurement period. The magnitude of the fluctuation shown in Fig. 16 (b) was estimated to be 2.3×10^{-6} T (standard deviation), while the average magnetic field was 1.2035462 T. A momentum dependence of the T_1' and T_1'' values also affects the statistical uncertainty of m_1/q_1 . As shown in Fig. 13(bottom), the momentum dependence of the T_1'' value remained observable. This dependence arises from the inaccurately known β or $B\rho$.

The uncertainty of T_0 depends on the quality of isochronous optics and timing resolution of the detectors. The main contribution to the uncertainty of T_0 stems from the optics imperfections, because the time resolution of the detectors was on the order of several tens of ps. The uncertainties were deduced to be $\delta(m_1/q_1)_{T_0} = 1.2 \times 10^{-6}$ u/q and 1.1×10^{-6} u/q

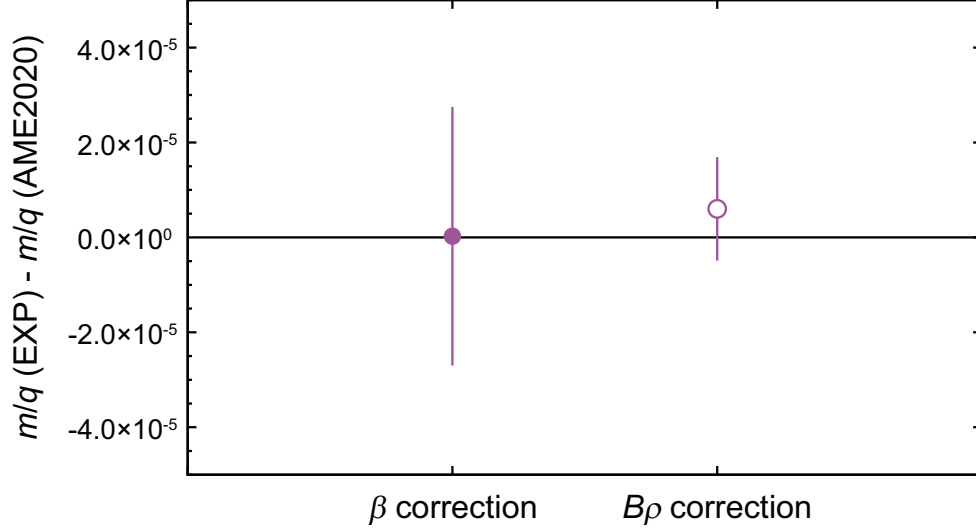


FIG. 15. Difference of the experimental ^{75}Cu m/q values for two correction methods and the literature value.

for the β and $B\rho$ corrections, respectively. The uncertainties of β , R , $B\rho_{\text{ring}}$, D_{F6} , and P_{F6avg} depend on the statistics and fitting procedure. The contributions of each uncertainty and the total uncertainties are listed in Table IV.

The total obtained uncertainties were $\delta(m_1/q_1)_\beta = 2.7 \times 10^{-5} \text{ u}/q$ and $\delta(m_1/q_1)_{B\rho} = 1.1 \times 10^{-5} \text{ u}/q$ for the β and $B\rho$ correction approaches, respectively. These values correspond to $\delta(m_1)_\beta = 740 \text{ keV}$ and $\delta(m_1)_{B\rho} = 290 \text{ keV}$. These uncertainties are about 10 times larger than the uncertainties of the upgraded isochronous mass measurements in CSRe [37, 39, 40], but comparable to the uncertainties of the original isochronous mass measurements in ESR [27, 28, 57].

Significant contributions to the total uncertainties were due to the statistical uncertainty of m_1/q_1 and uncertainty arising from the correction factor R in the β correction procedure. For the $B\rho$ correction routine, the statistical uncertainty m_1/q_1 was the main contributor to the total uncertainty. These results suggest that the improvement in the instabilities of the magnetic fields and the determination of accurate β and $B\rho$ values are essential. In this study, simple methods to obtain β and $B\rho$ were adopted. However, the analysis can be further improved to obtain more accurate β and/or $B\rho$.

TABLE IV. Uncertainties considered in the determination of the m_1/q_1 value for ^{75}Cu . Heading β and $B\rho$ stand for the employed correction method.

Contribution	β (u/q)	$B\rho$ (u/q)
$\delta(m_1/q_1)_{\text{sta}}$	1.3×10^{-5}	8.9×10^{-6}
$\delta(m_1/q_1)_{T_0}$	1.2×10^{-6}	1.1×10^{-6}
$\delta(m_1/q_1)_{\beta}$	6.7×10^{-6}	–
$\delta(m_1/q_1)_R$	2.3×10^{-5}	–
$\delta(m_1/q_1)_{B\rho_{\text{ring}}}$	–	3.3×10^{-6}
$\delta(m_1/q_1)_{D_{F6}}$	–	4.3×10^{-7}
$\delta(m_1/q_1)_{P_{F6\text{avg}}}$	–	5.1×10^{-6}
$\delta(m_1/q_1)$	2.7×10^{-5}	1.1×10^{-5}

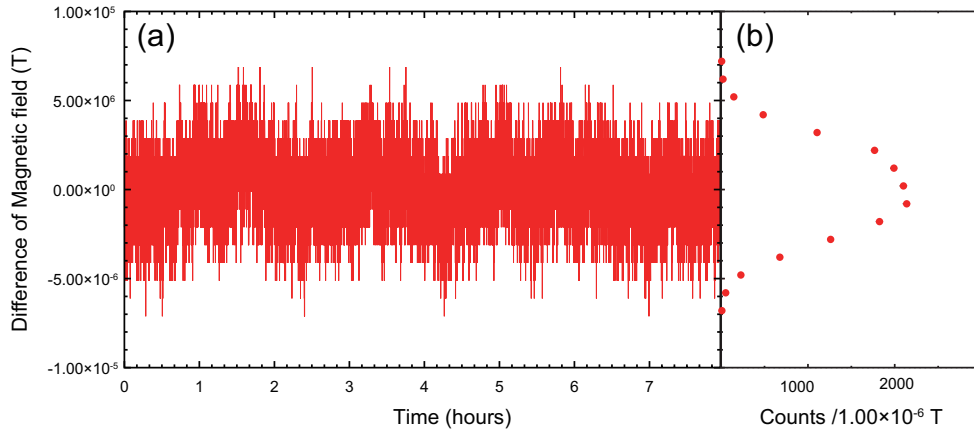


FIG. 16. (a) Time variation of the magnetic field. The differences from the average magnetic field are plotted. (b) The projection of Fig. 16 (a).

VI. CONCLUSION

This study describes the first isochronous mass spectrometry implemented in the Rare-RI Ring, which was conducted on nuclei with well-known masses and preceded the first mass measurements of new results reported in Ref. [43]. Individual-ion injection method, ion injection, storage, and extraction, together with TOF measurements in the ring applied to exotic nuclei have successfully been achieved. Consequently, the known mass of ^{75}Cu was re-measured under the strict conditions of short measurement durations. The measurement time of approximately 0.7 ms is excellently suited for pinning down yet unmeasured masses of the most exotic nuclei.

We established two analytical methods for the mass determination employing either β or $B\rho$ corrections. The obtained mass accuracies and uncertainties were on the order of the 10^{-6} u/ q and 10^{-5} u/ q , respectively for both, β and $B\rho$, correction methods. The major sources of the total uncertainty for the β correction analysis were the statistical uncertainty of m_1/q_1 and the uncertainty of R ; whereas for the $B\rho$ correction analysis, it was the statistical uncertainty of m_1/q_1 . The instabilities of the magnetic fields of the Rare-RI Ring and the momentum dependence of m_1/q_1 affected the statistical uncertainty of the m_1/q_1 value. This study suggests further improvements of the stability of the magnetic fields of the Rare-RI Ring to facilitate more accurate determination of β and $B\rho$ values.

Nonetheless, the obtained mass of ^{75}Cu is in satisfactory agreement with the literature value. The Rare-RI Ring facility has proved to be a powerful tool for mass measurements of rare RIs. Following the first results reported in [43], the Rare-RI Ring will be used for further mass measurements of short-lived nuclei, especially for nuclei involved in the r process.

VII. ACKNOWLEDGMENTS

The authors thank the accelerator staff of RIKEN Ring Cyclotron for support during the experiment. This experiment on the Rare-RI Ring was performed at the RI beam factory operated by RIKEN Nishina Center and CNS, University of Tokyo under the Experimental Program MS-EXP16-10. This work was supported by the RIKEN Pioneering Project funding and JSPS KAKENHI Grants No. 26287036, No. 25105506, No. 15H00830, and No. 17H01123. YAL received funding from the European Research Council (ERC) under

the European Union’s Horizon 2020 research and innovation programme (Grant Agreement No. 682841 “ASTRUM”).

- [1] T. Yamaguchi *et al.*, Masses of exotic nuclei, *Progress in Particle and Nuclear Physics* **120**, 103882 (2021).
- [2] John J. Cowan *et al.*, Origin of the heaviest elements: The rapid neutron-capture process, *Reviews of Modern Physics* **93**, 015002 (2021).
- [3] C.J. Horowitz *et al.*, r-process nucleosynthesis: connecting rare-isotope beam facilities with the cosmos, *Journal of Physics G: Nuclear and Particle Physics* **46**, 083001 (2019).
- [4] Darach Watson *et al.*, Identification of strontium in the merger of two neutron stars, *Nature* **574**, 497 (2019).
- [5] B.P. Abbott *et al.*, Multi-messenger Observations of a Binary Neutron Star Merger, *The Astrophysical Journal Letters* **848**, L12 (2017).
- [6] M. R. Drout *et al.*, Light curves of the neutron star merger GW170817/SSS17a: Implications for r-process nucleosynthesis, *Science* **358**, 1570 (2017).
- [7] B.P. Abbott *et al.* (LIGO Scientific Collaboration and Virgo Collaboration), GW170817: Observation of Gravitational Waves from a Binary Neutron Star Inspiral, *Phys. Rev. Lett.* **119**, 161101 (2017).
- [8] B. Sun *et al.*, Application of the relativistic mean-field mass model to the *r*-process and the influence of mass uncertainties, *Physical Review C* **78**, 025806 (2008).
- [9] D. Martin *et al.*, Impact of Nuclear Mass Uncertainties on the *r* Process, *Physical Review Letters* **116**, 121101 (2016).
- [10] X.F. Jiang *et al.*, Sensitivity Study of r-process Abundances to Nuclear Masses, *The Astrophysical Journal* **915**, 29 (2021).
- [11] Jens Dilling *et al.*, Penning-Trap Mass Measurements in Atomic and Nuclear Physics, *Annual Review of Nuclear and Particle Science* **68**, 45 (2018).
- [12] G. Bollen, Radioactive Ion Beams and Penning Traps, *Nuclear Physics A* **616**, 457c (1997).
- [13] J. Dilling *et al.*, The SHIPTRAP project: A capture and storage facility at GSI for heavy radionuclides from SHIP, *Hyperfine Interactions* **127**, 491 (2000).
- [14] V.S. Kolhinen *et al.*, JYFLTRAP: a cylindrical Penning trap for isobaric beam purification at IGISOL, *Nuclear Instruments and Methods in Physics Research Section A* **528**, 776 (2004).

- [15] R. Ringle *et al.*, Precision mass measurements with LEBIT at MSU, International Journal of Mass Spectrometry **251**, 300 (2006).
- [16] R.N. Wolf *et al.*, ISOLTRAP's multi-reflection time-of-flight mass separator/spectrometer, International Journal of Mass Spectrometry **349-350**, 123 (2013).
- [17] P. Schury *et al.*, A high-resolution multi-reflection time-of-flight mass spectrograph for precision mass measurements at RIKEN/SLOWRI, Nuclear Instruments and Methods in Physics Research B **335**, 39 (2014).
- [18] W.R. Plaß *et al.*, The FRS Ion Catcher - A facility for high-precision experiments with stopped projectile and fission fragments, Nuclear Instruments and Methods in Physics Research B **317**, 457 (2013).
- [19] Christian Jesch *et al.*, The MR-TOF-MS isobar separator for the TITAN facility at TRIUMF, Hype. Int. **235**, 97 (2015).
- [20] Yu.A. Litvinov *et al.*, Mass measurement of cooled neutron-deficient bismuth projectile fragments with time-resolved Schottky mass spectrometry at the FRS-ESR facility, Nuclear Physics A **756**, 3 (2005).
- [21] M. Hausmann *et al.*, First isochronous mass spectrometry at the experimental storage ring ESR, Nuclear Instruments and Methods in Physics Research Section A **446**, 569 (2000).
- [22] M. Hausmann *et al.*, Isochronous Mass Measurements of Hot Exotic Nuclei, Hyperfine Interactions **132**, 289 (2001).
- [23] X.L. Tu *et al.*, Precision isochronous mass measurements at the storage ring CSRe in Lanzhou, Nuclear Instruments and Methods in Physics Research Section A **654**, 213 (2011).
- [24] S. Baruah *et al.*, Mass Measurements beyond the Major *r*-Process Waiting Point ^{80}Zn , Physical Review Letters **101**, 262501 (2008).
- [25] B. Sun *et al.*, Nuclear structure studies of short-lived neutron-rich nuclei with the novel large-scale isochronous mass spectrometry at the FRS-ESR facility, Nuclear Physics A **812**, 1 (2008).
- [26] D. Atanasov *et al.*, Precision Mass Measurements of $^{129-131}\text{Cd}$ and Their Impact on Stellar Nucleosynthesis via the Rapid Neutron Capture Process, Physical Review Letters **115**, 232501 (2015).
- [27] R. K obel *et al.*, First direct mass measurements of stored neutron-rich $^{129,130,131}\text{Cd}$ isotopes with FRS-ESR, Physics Letters B **754**, 288 (2016).

- [28] R. K obel *et al.*, New results from isochronous mass measurements of neutron-rich uranium fission fragments with the FRS-ESR-facility at GSI, The European Physical Journal A **52**, 138 (2016).
- [29] M. Vilen *et al.*, Precision Mass Measurements on Neutron-Rich Rare-Earth Isotopes at JYFLTRAP: Reduced Neutron Pairing and Implications for *r*-Process Calculations, Physical Review Letters **120**, 262701 (2018).
- [30] Y. Yano, The RIKEN RI Beam Factory Project: A status report, Nuclear Instruments and Methods in Physics Research Section B **261**, 1009 (2007).
- [31] A. Ozawa *et al.*, The rare-RI ring, Progress of Theoretical and Experimental Physics **2012**, 03C009 (2012).
- [32] B. Franzke, The heavy ion storage and cooler ring project ESR at GSI, Nuclear Instruments and Methods in Physics Research Section B **24/25**, 18 (1987).
- [33] The heavy ion cooler-storage-ring project (HIRFL-CSR) at Lanzhou, Nuclear Instruments and Methods in Physics Research Section A", volume = "488", pages = "11–25", year = "2002", author = "J.W. Xia *et al.*", doi = "https://doi.org/10.1016/S0168-9002(02)00475-8".
- [34] Markus Steck and Yuri A. Litvinov, Heavy-ion storage rings and their use in precision experiments with highly charged ions, Progress in Particle and Nuclear Physics **115**, 103811 (2020).
- [35] H. Geissel and Yu.A. Litvinov, Precision experiments with relativistic exotic nuclei at GSI, Journal of Physics G: Nuclear and Particle Physics **31**, S1779 (2005).
- [36] H. Geissel *et al.*, A new experimental approach for isochronous mass measurements of short-lived exotic nuclei with the FRS-ESR facility, Hyperfine Interactions **173**, 49 (2006).
- [37] M. Wang *et al.*, $B\rho$ -defined isochronous mass spectrometry: An approach for high-precision mass measurements of short-lived nuclei, Phys. Rev. C **106**, L051301 (2022).
- [38] H. Geissel *et al.*, Novel isochronous features for FRS-ESR experiments with stored exotic projectile fragments, Nuclear Instruments and Methods in Physics Research Section B **541**, 305 (2023).
- [39] M. Zhang *et al.*, $B\rho$ -defined isochronous mass spectrometry and mass measurements of ^{58}Ni fragments, The European Physical Journal A **59**, 27 (2023).
- [40] X. Zhou *et al.*, Mass measurements show slowdown of rapid proton capture process at waiting-point nucleus ^{64}Ge , Nature Physics (2023).
- [41] M. Wang *et al.*, Mass Measurement of Upper fp -Shell $N = Z - 2$ and $N = Z - 1$ Nuclei and the Importance of Three-Nucleon Force along the $N = Z$ Line,

- Physical Review Letters **130**, 192501 (2023).
- [42] I. Meshkov *et al.*, Individual rare radioactive ion injection, cooling and storage in a ring, Nuclear Instruments and Methods in Physics Research Section A **523**, 262 (2004).
- [43] H.F. Li *et al.*, First Application of Mass Measurements with the Rare-RI Ring Reveals the Solar r -Process Abundance Trend at $A = 122$ and $A = 123$, Physical Review Letters **128**, 152701 (2022).
- [44] Y.H. Zhang *et al.*, Storage ring mass spectrometry for nuclear structure and astrophysics research, Physica Scripta **91**, 073002 (2016).
- [45] Toshiyuki Kubo, In-flight RI beam separator BigRIPS at RIKEN and elsewhere in Japan, Nuclear Instruments and Methods in Physics Research Section B **204**, 97 (2003).
- [46] S. Michimasa *et al.*, SHARAQ spectrometer for high-resolution studies for RI-induced reactions, Nuclear Instruments and Methods in Physics Research Section B **317**, 305 (2013).
- [47] T. Uesaka *et al.*, The high resolution SHARAQ spectrometer, Nuclear Instruments and Methods in Physics Research Section B **266**, 4218 (2008).
- [48] D. Nagae *et al.*, Development and operation of an electrostatic time-of-flight detector for the Rare RI storage Ring, Nuclear Instruments and Methods in Physics Research Section A **986**, 164713 (2021).
- [49] H. Miura *et al.*, Performance of a Fast Kicker Magnet for Rare-RI Ring, Part of Proceedings, 13th Heavy Ion Accelerator Technology Conference (HIAT2015) , MOPA23 (2015).
- [50] Shunichiro Omika *et al.*, Development of Experimental Devices for Precise Mass Measurements at the Rare-RI Ring Facility, JPS Conference Proceedings **35**, 011026 (2021).
- [51] S. Omika *et al.*, Development of a new in-ring beam monitor in the Rare-RI Ring, Nuclear Instruments and Methods in Physics Research Section B **463**, 241 (2020).
- [52] F. Suzaki *et al.*, Design study of a resonant Schottky pick-up for the Rare-RI Ring project, Nuclear Instruments and Methods in Physics Research Section B **317**, 636 (2013).
- [53] Meng Wang *et al.*, The AME 2020 atomic mass evaluation (II). Tables, graphs and references, Chinese Physics C **45**, 030003 (2021).
- [54] H. Kumagai *et al.*, Development of Parallel Plate Avalanche Counter (PPAC) for BigRIPS fragment separator, Nuclear Instruments and Methods in Physics Research Section B **317**, 717 (2013).
- [55] Acqiris - Time-to-Digital Converter TC842, .
- [56] ORTEC - Quad Constant-Fraction 200-MHz Discriminator 935, .

- [57] J. Stadlmann *et al.*, Direct mass measurement of bare short-lived ^{44}V , ^{48}Mn , ^{41}Ti and ^{45}Cr ions with isochronous mass spectrometry, *Physics Letters B* **586**, 27 (2004).